Nanoscale

PAPER

View Article Online
View Journal | View Issue

Cite this: *Nanoscale*, 2020, **12**, 18269

Unprecedented random lasing in 2D organolead halide single-crystalline perovskite microrods†

Pradip Kumar Roy, ‡[a] Rajesh Kumar Ulaganathan,‡[b] Chinnambedu Murugesan Raghavan,[c] Swapnil Milind Mhatre,[a] Hung-I Lin,[a] Wei-Liang Chen,[b] Yu-Ming Chang,[b] Alex Rozhin,[c] Yun-Tzu Hsu,[a] Yang-Fang Chen,[a] Raman Sankar, *[b,d] Fang-Cheng Chou *[b,e,f] and Chi-Te Liang *[a]

Three-dimensional organic–inorganic hybrid halide perovskites have been demonstrated as great materials for applications in optoelectronics and photonics. However, their inherent instabilities in the presence of moisture, light, and heat may hinder their commercialization. Alternatively, emerging two-dimensional (2D) organic–inorganic hybrid perovskites have recently attracted increasing attention owing to their great environmental stability and inherent natural quantum-well structure. In this work, we have synthesized a high-quality long-chain organic diammonium spacer assisted 2D hybrid perovskite FA-(*N*-MPDA)$PbBr_4$ (FA = formamidinium and *N*-MPDA = *N*-methylpropane-1,3-diammonium) by the slow evaporation at constant temperature method. The millimeter-sized single-crystalline microrods demonstrate low threshold random lasing behavior at room temperature. The single-crystalline 2D hybrid perovskite random laser achieved a very narrow linewidth (~0.1 nm) with a low threshold (~0.5 μJ cm^{-2}) and a high quality factor (~5350). Furthermore, the 2D hybrid microrod laser shows stable lasing emission with no measurable degradation after at least 2 h under continuous illumination, which substantially proves the stability of 2D perovskites. Our results demonstrate the promise of 2D organic–inorganic microrod-shaped perovskites and provide an important step toward the realization of high-performance optoelectronic devices.

Received 10th February 2020,
Accepted 29th July 2020

DOI: 10.1039/d0nr01171a

rsc.li/nanoscale

Organolead halide hybrid perovskites have recently emerged as promising materials due to their wide range of applications in photodetectors, field-effect transistors, solar cells, and a newly added application, random lasers.[1,2] Typically, organic–inorganic hybrid perovskites are represented by a three-dimensional (3D) lattice framework with chemical formula ABX_3 (A = MA/FA and B = Pb). They have excellent light-absorbing characteristics with optically tunable band gaps and have attracted considerable interest, especially in the photovoltaic industry for solar cell device fabrication, due to their low cost and simple large-scale production. Within a short time of their introduction, perovskite solar cells (PSCs) achieved above 20% power conversion efficiency (PCE). But the lack of uniformity, defects in the grain boundary/interfacial regions, and the poor reproducibility of PSCs are major challenges for obtaining highly stable devices with efficient performances. To overcome these issues, various approaches have been employed, such as introducing superalkali atoms,[3] CdSe quantum dot/PCBM composites as the electron transport layer,[4] and passivation using a poly-triarylamine layer.[5] These strategies have expanded the family of PSCs. However, these 3D perovskite structures are prone to thermal, moisture, and light-induced degradation, which cause irreversible performance fading.[6–8] In contrast, two-dimensional (2D) organic–inorganic hybrid perovskites are materials with inherent multiple quantum well (QW) structures,[9,10] which provide unique and promising advantages as compared to their 3D counterparts,[11] including both photo-/chemical stability and quantum tunable optoelectronic properties.[12] 2D perovskites are composed of an in-

[a]*Department of Physics, National Taiwan University, Taipei 10617, Taiwan. E-mail: ctliang@phys.ntu.edu.tw*
[b]*Center for Condensed Matter Sciences, National Taiwan University, Taipei 10617, Taiwan. E-mail: sankarndf@gmail.com, fcchou@ntu.edu.tw*
[c]*Nanoscience Laboratory, Aston Institute of Photonic Technologies, Aston University, Birmingham B4 7ET, UK*
[d]*Institute of Physics, Academia Sinica, Taipei 11529, Taiwan*
[e]*Taiwan Consortium of Emergent Crystalline Materials, Ministry of Science and Technology, Taipei 10622, Taiwan*
[f]*Center of Atomic Initiative for New Materials, National Taiwan University, Taipei 10617, Taiwan*

†Electronic supplementary information (ESI) available: A brief description of the SECT growth method, EDX analysis, below threshold PL emission, Tauc plot with binding energy calculations, and *Q*-factor calculations. See DOI: 10.1039/d0nr01171a

‡These authors contributed equally.

organic part and an organic part. The inorganic perovskite slabs form the 2D conducting layers that are sandwiched between organic barrier layers to form a natural QW structure. The dielectric constant difference between the inorganic and organic layers leads to effective confinement of electron–hole pairs within the QW-like 2D perovskite system, which further induces excitons with a high binding energy that are stable at room temperature. Their larger cations hamper interionic motion whereas the organic moieties confer hydrophobicity which increases their moisture tolerance.[13] The properties of perovskites can be tuned easily by changing their '*n*' value, which essentially gives the number of inorganic layers.[13,14] Moreover, the value of '*n*' determines the width of the QW which leads to significant exciton formation with large binding energy. Compared to polycrystalline thin films, hybrid perovskites in single-crystal form have the advantage of exceptionally long carrier diffusion length because of their lower trap densities, improved charge transport, high absorption, and reduced defects due to large grain boundaries. Therefore, it is vital to search for novel growth methods for preparing single-crystal hybrid perovskites suitable for future optoelectronics.

There are several methods of growing hybrid perovskites reported in the literature, such as slow cooling,[15] inverse temperature crystallization (ITC),[16] and anti-solvent vapor diffusion (ASVD).[17] However, the growth of large-sized single crystals by these techniques is very complicated due to the presence of large organic moieties and long-chain molecules, as well as the possibility of the formation of multi-stacking crystals with random crystallization. In order to overcome these issues, the slow evaporation at constant temperature (SECT) solution growth method has been employed, which efficiently controls the rapid nucleation and reduces the multi-crystallinity of the perovskites, to grow millimeter- to centimeter-sized single crystals.[18] Currently, to the best of our knowledge, there is no report on the single-crystal growth of *N*-MPDA based 2D perovskites. To this end, we have focused on the single-crystal growth of (*N*-MPDA)$PbBr_4$ perovskites with the incorporation of formamidinium (FA) into (*N*-MPDA)$PbBr_4$ to achieve a stable 2D layered FA-(*N*-MPDA)$PbBr_4$ perovskite system. Generally, the stability of perovskites depends on the Goldschmidt tolerance factor (t),[19–21] which is defined as $t = r_A + r_X/\sqrt{2}(r_B + r_X)$. Here, r_A and r_B are the ionic radii of the A and B cations, and r_X is the ionic radius of the anion. A higher value of t implies higher stability due to the increased symmetry of the perovskite structure. The tolerance factor of the perovskite is improved by the incorporation of larger ions into the perovskite lattice, which brings several advantages, particularly for maintaining the perovskite crystal symmetry and thermal stability. There are many reports which demonstrate the replacement of the MA^+ ion by the FA^+ ion in order to increase the stability of both single crystals and polycrystalline thin films.[22,23]

2D perovskites attract a great deal of attention due to their applications in optoelectronics. In a recent report, it has been confirmed that *N*-MPDA is an excellent candidate for warm and cold white LEDs due to its broadband emission over the entire visible spectrum.[24] This phenomenon inspired our focus on fabricating emerging random laser devices using microrod-shaped FA-(*N*-MPDA)$PbBr_4$ 2D perovskite single crystals. Random lasers exhibit several advantages as compared to conventional lasers, which require a gain medium to amplify the light and an optical cavity for the amplification to be efficient. In contrast, a random laser does not require a separate medium; the material itself acts as a gain medium for optical feedback.[25] The gain is provided by the scattering of light which occurs due to the randomness. The light can diffuse and randomly forms closed loops by constructive interference to realize the lasing modes. The major advantage of random lasers lies in their inexpensive and relatively simple technology compared to that of regular lasers. The properties that make random lasers special compared to regular lasers are their color and angular dependence over the complete solid angle of 4π, which makes them ideal candidates for display applications.[25] In addition, random lasers have a unique characteristic, namely the coexistence of high temporal coherence and low spatial coherence, which makes random lasers an ideal light source for speckle-free imaging.[26] These fascinating phenomena of random lasing can lead to different potential applications, such as superbright lighting devices, display systems, Li-Fi, speckle-free imaging technology, *etc*. Our primary motivation is to achieve efficient ultra-low threshold random lasers. Several ingredients are necessary to accomplish ultra-low threshold lasing: (i) a high-quality gain medium with slow non-radiative decay pathways at the carrier density levels for population inversion, (ii) high mobilities and free-carrier densities to minimize resistive heat loss, (iii) good thermal stability, and (iv) a large gain cross-section at the lasing wavelength and sharp band tails. Remarkably, perovskites have exhibited all the aforementioned attributes. Furthermore, utilizing the single-crystalline properties of perovskites, owing to the low trap-state density and long Auger lifetimes, the resultant lasers can demonstrate low lasing thresholds with very high quality factor. Recently, 3D hybrid ABX_3 perovskites in the form of thin films, microdisks, nanoplatelets, and quantum dots have been reported as efficient optical gain media for lasing.[27–32] Nevertheless, room-temperature optical gain and laser behavior are very rare in 2D layered perovskites, which encourages us to explore the possible lasing behavior of 2D FA-(*N*-MPDA)$PbBr_4$ single crystals.

In this work, we demonstrate room-temperature lasing of 2D perovskite microrods with a low threshold (~0.5 μJ cm^{-2}), high quality factors, and excellent photostability in an ambient air environment. The lasing mode linewidth can exhibit an ultra-low value of 0.1 nm and the corresponding quality factor can be as high as 5350, which is the highest among single-crystalline perovskites. The remarkable performance of the 2D hybrid perovskite microrods can be attributed to a high absorption coefficient, high quality factor, 2D quantum confinement, and low non-radiative recombination rates. We believe that our single-crystalline 2D perovskites will

pave the way towards the development of solution-based low threshold laser sources.

Results and discussion

Fig. 1a demonstrates a schematic illustration of the SECT technique for the growth of millimeter-size single-crystalline perovskite microrods. This solution growth technique controls the rapid nucleation and reduces the multi-crystallinity of the perovskites to obtain high-purity single crystals (Fig. S1†). The step-by-step growth process is described as follows. Initially, a saturated solution of FA-(*N*-MPDA)$PbBr_4$ is prepared by dissolving as-synthesized FA-(*N*-MPDA)$PbBr_4$ at 120 °C (Step 1), under constant magnetic stirring. The saturated solution was stabilized for one hour with continuous stirring to ensure that there were no undissolved minute particles. The solution was then subjected to controlled evaporation in an oil bath at a constant temperature to attain supersaturation (Step 2). During the nucleation process, the excess solute present in the supersaturated solution crystallizes at the bottom (Step 3). We further optimized our saturated solution and allowed a slow evaporation process for 1 day at a constant temperature to attain the high-quality single-crystalline microrod-shaped perovskite. Fig. 1b displays an optical image of an as-synthesized single-crystalline FA-(*N*-MPDA)$PbBr_4$ microrod, which exhibits a yellowish color. The length and diameter of the crystalline rod are millimeter- and micrometer-sized, respectively (3 mm and 2 μm). The inset of Fig. 1b shows a top-view SEM image of an as-grown millimeter-size perovskite microrod. X-ray diffraction (XRD) characterization was performed on the as-grown perovskite rods to study the crystal structure and purity (as shown in Fig. 1c, Fig. S2†). The XRD pattern shows strong diffraction peaks with regular interplanar spacing at 2θ values of 9.08°, 18.18°, 27.25°, 36.63°, 46.20°, 56.15°, and 66.42°, which are assigned to the (002), (004), (006), (008), (0010), (0012), and (0014) lattice planes, respectively. These diffraction peaks indicate that the surface has a preferred orientation in the *c*-direction, since they were indexed to the (00*l*) planes. The periodic repetitions of the Miller planes reveal the single-crystallinity as well as the layered structure of the FA-(*N*-MPDA)$PbBr_4$ perovskite.[31] The lattice parameter values are determined to be a = 12.83 Å, b = 5.94 Å and c = 13.17 Å with a space group of $P2/m$. An as-grown FA-(*N*-MPDA)$PbBr_4$ microrod crystal was further examined by energy-dispersive X-ray spectroscopy to assess the chemical uniformity. From the EDX mapping (Fig. S3†), the even distribution of C, N, Pb, and Br atoms in the single-crystalline microrod is confirmed. The EDX spectrum of the FA-(*N*-MPDA)$PbBr_4$ microrod is displayed in Fig. S4,† and shows prominent individual peaks for all atoms. The crystallinity of the FA-(*N*-MPDA)$PbBr_4$ microrods was investigated by selected area electron diffraction (SAED). The SAED pattern shows that the as-grown FA-(*N*-MPDA)$PbBr_4$ microrods are of good quality and are crystalline in nature (Fig. 1d). In addition, high resolution transmission electron microscopy (HR-TEM) was performed as shown in Fig. 1e, which confirms that the spacing between the lattice fringes is about 0.25 nm. Photoluminescence (PL) experiments were performed to characterize the optical properties and to understand the uniformity of the single crystals. The microrods were transferred to a clean glass plate substrate and excited by an 8 MHz 405 nm pulsed laser. The PL measurements were carried out with a 10× objective and 3 μW power irradiation of the sample. Fig. 2a shows a typical emission spectrum with an

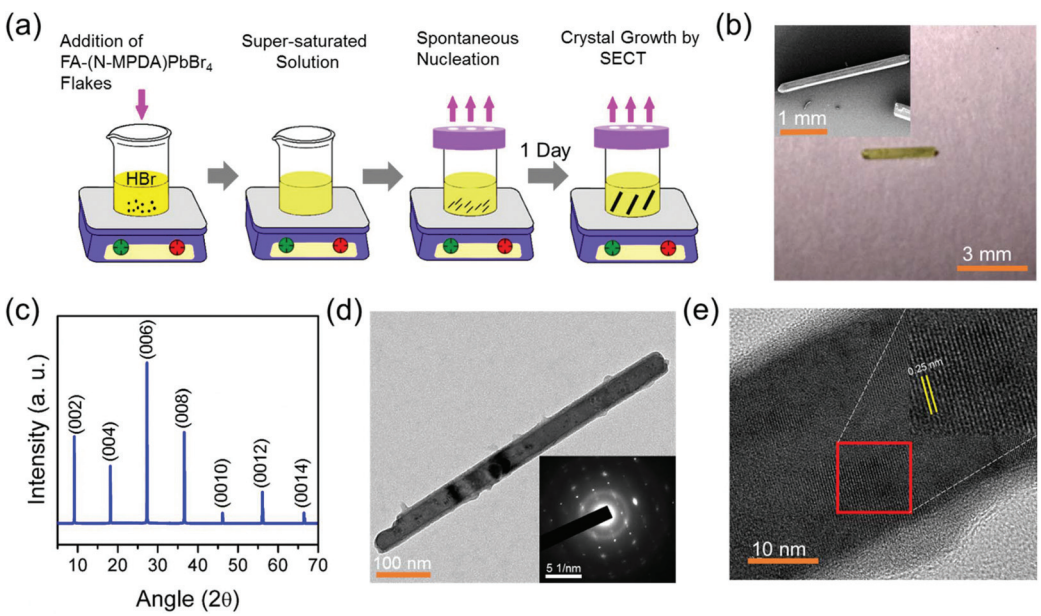

Fig. 1 (a) Schematic illustration of the synthesis of FA-(*N*-MPDA)$PbBr_4$ microrods. (b) Optical image of an as-synthesized microrod ~3 mm in length (inset: top-view SEM image of the microrod). (c) XRD pattern of 2D microrods. (d) TEM image of an FA-(*N*-MPDA)$PbBr_4$ microrod at lower magnification with the SAED pattern (inset). (e) An HR-TEM image of an FA-(*N*-MPDA)$PbBr_4$ microrod is displayed with lattice fringes of about 0.25 nm.

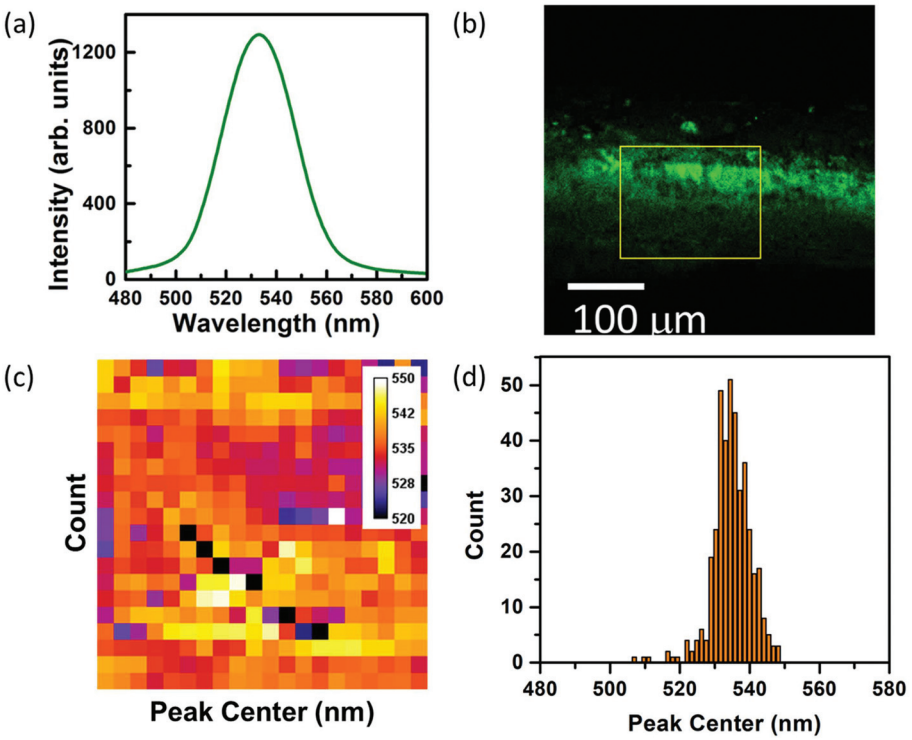

Fig. 2 (a) The emission spectrum of the as-synthesized microrods with a peak centered at 535 nm. (b) PMT mapping of a microrod with the yellow rectangle showing the area used for spectral mapping. (c and d) Peak center mapping and the corresponding histogram distribution of the yellow rectangular area shown in (b). The mapping confirms the microrod uniformity.

emission peak centered at 535 nm. The Photomultiplier tube (PMT) mapping image of a microrod is shown in Fig. 2b. PL spectral mapping was conducted over the rectangular marked area. The emission peak center of the spectral mapping is illustrated in Fig. 2c, where different colors represent the peak center values of the mapping area. It is found that the emission peak centers are uniformly distributed over the crystal, confirming that the as-grown FA-(*N*-MPDA)$PbBr_4$ microrods are of good quality.[18,33] The histogram of the emission peak demonstrates a distribution centered at ~535 nm (Fig. 2d). The sharp spectrum reveals the excellent optical quality of the single-crystalline microrods.[18]

A schematic illustration of the generation of random lasers *via* 2D perovskite single crystals is depicted in Fig. 3a. Although we have single-crystalline perovskite microrods as evidenced by the XRD results, it is inevitable that there are some defects and dislocations in our large-size (3 mm × 2 μm) sample. These crystal imperfections, together with the surfaces of our single-crystal microrods which can be considered as the grain boundaries, behave as scattering centers, where the spontaneously emitted photons are scattered in all directions. Some Fabry–Pérot-like peaks (when light bounces back and forth along the crystal) may well co-exist with the random lasing ones. After multiple scattering, closed loops are formed inside the optical gain media and provide coherent feedback to the emission *via* constructive interference.[34] As a result, laser action is achieved. As shown in Fig. 3b and Fig. S5,† multiple sharp lasing peaks have been observed, even for spectrally close lasing modes. This can be attributed to the fact that the lasing modes overlap very weakly due to their exponential confinement.[35] There is a large difference in refractive index at the end facets between the organic–inorganic hybrid single-crystalline perovskite rod and the outside environment,[36] which itself can act as a gain medium, leading to a very small critical angle for total internal reflection inside the crystal. This fascinating feature enhances the light-trapping probability inside the crystal, which may ensure further enhancement of the internal light scattering.

The random lasing action was studied under excitation by a 374 nm pulsed laser with a frequency of 40 MHz and a pulse width of 55 ps. Fig. 3b shows the evolution of the PL spectrum as a function of pumping energy density. At low pumping energies, the PL spectra show a broad emission profile with a nearly Gaussian shape and a high full width at half maximum (FWHM) of ~25 nm (Fig. S6†). When the incident power exceeds the threshold (P_{th}), the spectra start showing sharp emission peaks, which indicates the transition from spontaneous emission to stimulated emission. It is worth mentioning that multiple sharp peaks of the random laser can be seen throughout the whole spectrum, which might be quite interesting for display applications. The multiple peaks in the spectra signify the number of modes with interference providing substantial feedback. The FWHM ($\delta\lambda$) of individual lasing peaks of the dominant lasing mode is as low as ~0.1 nm (fitted by a

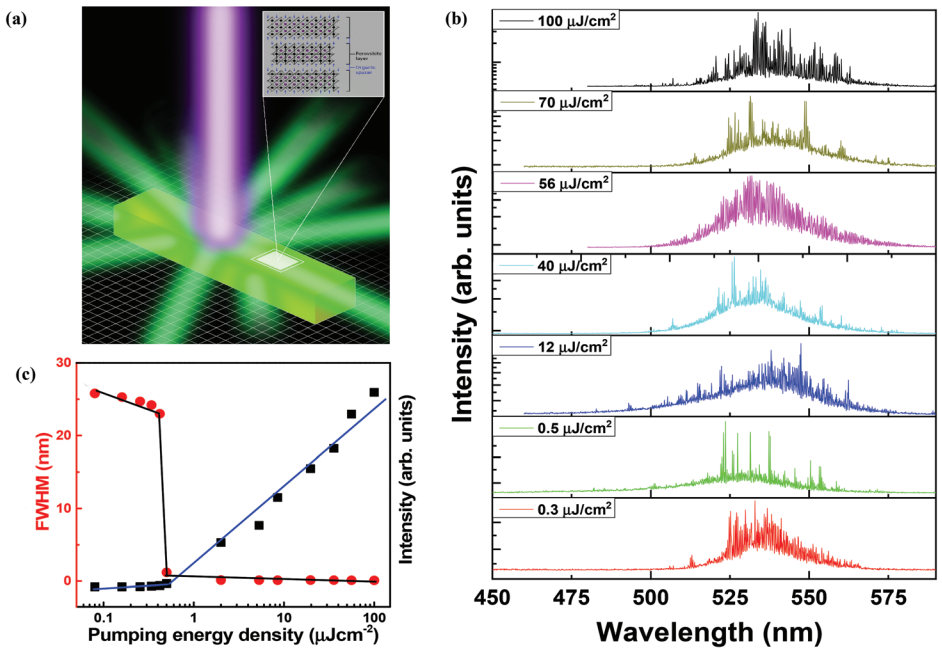

Fig. 3 (a) Schematic illustration of random lasers in a single-crystalline 2D perovskite microrod. The enlarged picture illustrates the multiple quantum wall structure formed by the organic and inorganic molecules in the 2D perovskite. (b) Random lasing from a 2D perovskite single-crystal microrod on a semi-log scale. Evolution of the emission spectrum of the 2D perovskite device as a function of pumping energy density. (c) Integrated intensity and emission line width as a function of pump fluence. A clear linewidth narrowing occurs near the threshold of P_{th} = 0.5 μJ cm^{-2}, accompanied by a sharp increase in emission intensity.

Gaussian function, Fig. S7†), which gives rise to a high cavity quality factor of ~5350 (at 535 nm emission wavelength) calculated by using the relationship $Q = \lambda/\delta\lambda$ (ESI†). As a side note, the most important characteristic of a laser device, the spectral coherence, can be evaluated using the lasing linewidth. As described by the Schawlow–Townes equation, the lasing linewidth is constrained by the Q factor and gain value of the semiconductor, and the coupling efficiency of spontaneous emission into the lasing process.[37] A plot of the spectral linewidth and intensity *vs.* the pumping energy density can be seen in Fig. 3c. The threshold value of pumping energy density is as low as 0.5 μJ cm^{-2}. Beyond the threshold value, we can see that the FWHM decreases drastically from 25 nm to 0.1 nm. The narrowing of the emission peak in the spectra is proof of significant lasing action. The low threshold of the random laser can be attributed to the large exciton binding energy (~300 meV (Fig. S8†))[13] of the 2D hybrid single-crystalline rod and the scattered light, which may form coherent feedback loops inside the 2D single crystal. The threshold value for a random laser is known to be inversely proportional to the mean free path of the emitted photons. Owing to their highly crystalline nature and low trap state density, 2D single crystals are known to have a long mean free path and hence a very low lasing threshold.[38] Also, it is reported that to attain a lower pumping threshold energy value, the Auger recombination should be much slower.[39,40] The single-crystal structure exhibits much slower Auger recombination compared to that of colloidal perovskites, which helps to decrease the lasing threshold.

To verify the characteristics of the random lasing action, we conducted angle-dependent PL measurements and examined the area dependence of the emission spectrum. Fig. 4a displays the emission spectra at different angles ranging from −20° to +20°, where the collection angles are achieved by vertically rotating the sample with respect to the line of incidence of the pumping laser as shown in the insets of Fig. 4a. Quite interestingly, the achieved spectra show lasing phenomena at each measured angle, which provides firm evidence of the random lasing behavior and confirms the multi-directionality of the random laser output. The localization of light is not always in the same direction or the same path, hence different localization paths will result in random lasing with different directions. It is important to mention that the number of laser modes for both rotation angles (−20° and +20°) decreases compared to a 0° rotation. This phenomenon is expected, as the tiling of the sample changes the random media in terms of gain. Due to this reason, the modes will be different.[41] We have recorded the laser spectrum with different objective lenses to study the dependence of the emitted spectrum on pumping laser spot size with a fixed incident energy density of 12 μJ cm^{-2} as shown in Fig. 4b and Fig. S9.† We collected the emission spectrum using different objective lenses, 60× and 100×, corresponding to illumination areas of 23.80 and 12.56 μm^2, respectively. These results show that with an increase in excitation area, the lasing peaks are found to be stronger, as more closed-loop paths for the emitted photons can be formed in a larger excitation volume.[42] Alternatively, the number of modes observed with a 100× lens is increased

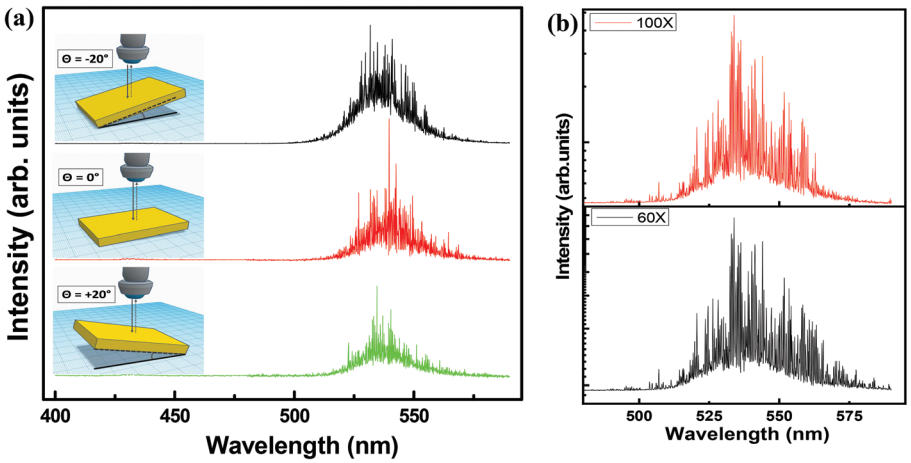

Fig. 4 Evidence of random lasing from a 2D perovskite single-crystalline microrod. (a) Angular dependence of lasing emission spectra recorded at a constant pump fluence of 12 μJ cm^{-2}. The angles +20, 0, and −20 degrees are achieved by vertically rotating the sample with respect to the line of incidence of the pumping laser as shown in the insets of the respective spectra. The lines serve as a guide to the eye. (b) Effect of variation of the laser spot size on the emitted spectrum on a semi-log scale while keeping the power density fixed at 12 μJ cm^{-2}.

with increasing pumping energy density, as shown in Fig. 3b, as saturation of the number of modes has not been achieved.[43] The random laser model fits quite well with the observed emitted spectra.

The ambient stability of random laser devices is one of the essential parameters for their practical application. In order to prove the ambient stability of our device, we have recorded the emission spectra and microscopy images of our random laser device over time as shown in Fig. 5. Fig. 5b shows that the shape and intensity of the microscopy images remained unchanged with time. The intensity of the laser spectrum remained stable for more than two hours under ambient conditions as shown in Fig. 5a, which attested the stability of our 2D perovskite. In short, the multiple time observations of the laser action from a single point on the device demonstrate the stable lasing action of the device,[44] which can be attributed to the stable and fascinating optical properties of 2D single-crystalline perovskites.

In order to further demonstrate the dynamic process of the lasing action, we performed time-resolved photoluminescence (TRPL) studies at different pumping energy densities of the same excitation source. The TRPL decay curves at different excitation fluences ranging from PL to random lasing processes are illustrated in Fig. 6a. We further plot the obtained excited state carrier lifetime as a function of pumping energy density in Fig. 6b. At lower pumping energy fluences (less than the threshold), the decay profile fitted by an exponential function yields a lifetime of ~4.5 ns, whereas a very fast decay time of ~0.12 ns is obtained when the excitation fluence is above the threshold. This phenomenon indicates the occurrence of a stimulated emission process and lasing action in the 2D perovskite device (Fig. 3b). Such a low lifetime can be attributed

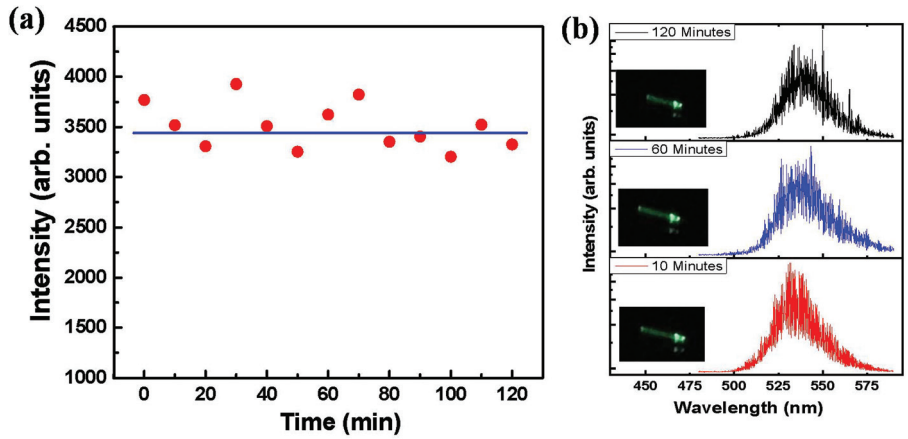

Fig. 5 Random lasing stability measurements on a 2D perovskite single-crystalline microrod. (a) Lasing (centered at ~535 nm) under pumping at 374 nm with a fluence of 12 μJ cm^{-2} with time. (b) Random lasing spectra and microscopy images recorded at a constant pump fluence of 12 μJ cm^{-2} as a function of time.

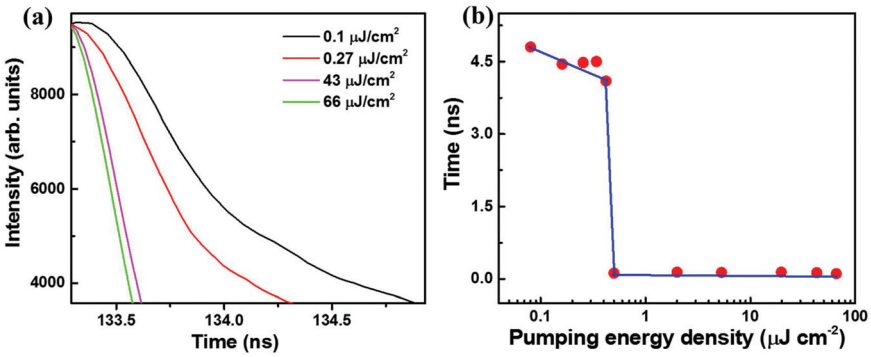

Fig. 6 Lifetime measurements on a 2D perovskite single-crystalline microrod. (a) Typical PL dynamics observed at different pumping energy densities. (b) Calculated excited state carrier lifetime as a function of pumping energy density. An obvious lifetime change occurs near the threshold of P_{th} = 0.5 μJ cm^{-2}.

to a higher recombination rate as there are a larger number of modes available. It is well known that the radiation density is directly proportional to the recombination rate in the matrix, and due to this reason the abrupt decrease in carrier lifetime at the threshold pumping energy signifies a stimulated emission process and provides strong evidence of lasing occurrence.[44,45]

Conclusion

We have successfully grown a millimeter-sized high-quality 2D single-crystal perovskite (FA-(*N*-MPDA)PbBr$_4$) using the SECT solution growth technique. The 2D hybrid single crystals exhibit a high crystallinity with a well-defined rod-shaped structure, resulting in good optical properties with a uniform emission center at 535 nm over the entire region. The random lasing properties of the 2D single-crystal perovskite have been investigated, which revealed long-term stability over 2 hours under ambient atmosphere. To the best of our knowledge, this is the first attempt at designing a laser device based on a single-crystalline FA-(*N*-MPDA)PbBr$_4$ microrod structure, which demonstrates a significant reduction in laser threshold (0.5 μJ cm^{-2}) with a very narrow lasing linewidth (0.1 nm) and a superior quality factor of 5350 (at 535 nm emission wavelength). The low threshold can be attributed to the strong quantum confinement, long mean free path, and large exciton binding energy of the 2D single-crystal perovskite. The unprecedented and versatile optical performance together with the 2D single-crystalline structure may hold the key to realizing solution-processed random lasing for future optoelectronic exploration and development.

Experimental section

Preparation of precursor material and single-crystal growth of FA-(*N*-MPDA)PbBr$_4$

For the preparation of the precursor material, the raw materials lead oxide (PbO), hydrobromic acid (HBr), *N*-methylpropane-1,3-diammonium ($CH_3NH(CH_2)_3NH_2$) (*N*-MPDA), and formamidinium chloride ($HC(NH_2)_2Cl$) were used. All the chemicals were high purity and were purchased from Sigma Aldrich. Initially, PbO (10 mmol) was dissolved in HBr at 70 °C under continuous stirring until the formation of a clear bright yellow solution. In parallel, $CH_3NH(CH_2)_3NH_2$ (3.33 mmol) was added dropwise into an HBr solution with continuous stirring to form an (*N*-MPDA)$^+$Br$^-$ salt solution. The above neutralization reaction is exothermic; therefore, it was carried out in an ice bath. To obtain the 2D (*N*-MPDA)PbBr$_4$ perovskite, the neutralized cold salt solution of (*N*-MPDA)$^+$Br$^-$ was added into the hot PbO solution at 120 °C. A yellow precipitate started to form, which was redissolved by continuous stirring followed by the addition of a slight excess of HBr solution to get a clear bright yellow solution. The final solution was allowed to rest for slow evaporation at a constant temperature to obtain the (*N*-MPDA)PbBr$_4$ perovskite compound. For the synthesis of the FA-(*N*-MPDA)PbBr$_4$ perovskite material, FACl was added into the PbO solution first, followed by dropwise addition of the (*N*-MPDA)$^+$Br$^-$ solution with continuous stirring. To obtain a millimeter-sized crystal, we followed the SECT growth technique in which the supersaturated solution was allowed to undergo slow evaporation at a constant temperature over 1 day. During the nucleation, the excess solute in the supersaturated solution started to crystallize at the bottom of the beaker to form a crystal with a larger size.

Characterization

The XRD pattern was obtained with a Bruker D2 PHASER diffractometer (CuKα radiation). Scanning electron microscopy (SEM) and energy-dispersive X-ray spectroscopy (EDX) mapping (FEI, Nova 200) were performed to analyze the morphology and chemical constituents of the FA-(*N*-MPDA)PbBr$_4$ perovskite single crystals. A pulsed laser of wavelength 374 nm was used as the pumping source for studying the lasing spectra and carrier lifetime. A Horiba–Jobin–Yvon TRIAX 320 spectrometer with 100× objective was used as the signal collector. The laser incident area dependent lasing spectra were acquired using a Horiba–Jobin–Yvon TRIAX 320 spectrometer

with 60× (LMPlanFI, Japan) and 100× (Olympus, Japan) objectives.

Author contributions

The manuscript was written through contributions from all authors. All authors have given their approval to the final version of the manuscript.

Conflicts of interest

There are no conflicts to declare.

Acknowledgements

This work was supported by the Ministry of Science and Technology (MOST), Taiwan under grant numbers MOST 109-2124-M-002-001, MOST 108-2112-M-001-049-MY2, and MOST 108-2119-M-002-025-MY3, Academia Sinica funded i-MATE financial support AS-iMATE-109-13 and the Ministry of Education, Taiwan. RCM and AR want to thank the support from the Marie Skłodowska-Curie Individual Fellowship (MOFUS, # 795356).

References

1 X. Gao, X. Zhang, W. Yin, H. Wang, Y. Hu, Q. Zhang, Z. Shi, V. L. Colvin, W. W. Yu and Y. Zhang, *Adv. Sci.*, 2019, **6**, 1900941.
2 M. Liu, H. Zhang, D. Gedamu, P. Fourmont, H. Rekola, A. Hiltunen, S. G. Cloutier, R. Nechache, A. Priimagi and P. Vivo, *Small*, 2019, **15**, 1900801.
3 M. Wang, H. Wang, W. Li, X. Hu, K. Sun and Z. Zang, *J. Mater. Chem. A*, 2019, **7**, 26421–26428.
4 X. Zeng, T. Zhou, C. Leng, Z. Zang, M. Wang, W. Hu, X. Tang, S. Lu, L. Fang and M. Zhou, *J. Mater. Chem. A*, 2017, **5**, 17499.
5 T. Zhou, M. Wang, Z. Zang and L. Fang, *Adv. Energy Mater.*, 2019, **9**, 1900664.
6 I. C. Smith, E. T. Hoke, D. Solis-Ibarra, M. D. McGehee and H. I. Karunadasa, *Angew. Chem., Int. Ed.*, 2014, **53**, 11232.
7 D. H. Cao, C. C. Stoumpos, O. K. Farha, J. T. Hupp and M. G. Kanatzidis, *J. Am. Chem. Soc.*, 2015, **137**, 7843.
8 C. Ma, C. Leng, Y. Ji, X. Wei, K. Sun, L. Tang, J. Yang, W. Luo, C. Li, Y. Deng, S. Feng, J. Shen, S. Lu, C. Du and H. Shi, *Nanoscale*, 2016, **8**, 18309.
9 T. Zhou, M. Wang, Z. Zang, X. Tang and L. Fang, *Sol. Energy Mater. Sol. Cells*, 2019, **191**, 33.
10 H. Tsai, W. Nie, J.-C. Blancon, C. C. Stoumpos, R. Asadpour, B. Harutyunyan, A. J. Neukirch, R. Verduzco, J. J. Crochet, S. Tretiak, L. Pedesseau, J. Even, M. A. Alam, G. Gupta, J. Lou, P. M. Ajayan, M. J. Bedzyk, M. G. Kanatzidis and A. D. Mohite, *Nature*, 2016, **536**, 312.
11 J. Chen, Y. Wang, L. Gan, Y. He, H. Li and T. Zhai, *Angew. Chem., Int. Ed.*, 2017, **56**, 14893.
12 C. R. Kagan, D. B. Mitzi and C. D. Dimitrakopoulos, *Science*, 1999, **286**, 945.
13 J.-C. Blancon, H. Tsai, W. Nie, C. C. Stoumpos, L. Pedesseau, C. Katan, M. Kepenekian, C. M. M. Soe, K. Appavoo, M. Y. Sfeir, S. Tretiak, P. M. Ajayan, M. G. Kanatzidis, J. Even, J. J. Crochet and A. D. Mohite, *Science*, 2017, **355**, 1288.
14 C. C. Stoumpos, D. H. Cao, D. J. Clark, J. Young, J. M. Rondinelli, J. I. Jang, J. T. Hupp and M. G. Kanatzidis, *Chem. Mater.*, 2016, **28**, 2852.
15 W. Peng, J. Yin, K.-T. Ho, O. Ouellette, M. De Bastiani, B. Murali, O. El Tall, C. Shen, X. Miao, J. Pan, E. Alarousu, J.-H. He, B. S. Ooi, O. F. Mohammed, E. Sargent and O. M. Bakr, *Nano Lett.*, 2017, **17**, 4759.
16 G. Maculan, A. D. Sheikh, A. L. Abdelhady, M. I. Saidaminov, M. A. Haque, B. Murali, E. Alarousu, O. F. Mohammed, T. Wu and O. M. Bakr, *J. Phys. Chem. Lett.*, 2015, **6**, 3781.
17 D. Shi, V. Adinolfi, R. Comin, M. Yuan, E. Alarousu, A. Buin, Y. Chen, S. Hoogland, A. Rothenberger, K. Katsiev, Y. Losovyj, X. Zhang, P. A. Dowben, O. F. Mohammed, E. H. Sargent and O. M. Bakr, *Nano Lett.*, 2015, **347**, 519.
18 C. M. Raghavan, T.-P. Chen, S.-S. Li, W.-L. Chen, C.-Y. Lo, Y.-M. Liao, G. Haider, C.-C. Lin, C.-C. Chen, R. Sankar, Y.-M. Chang, F.-C. Chou and C.-W. Chen, *Nano Lett.*, 2018, **18**, 3221.
19 C. J. Bartel, C. Sutton, B. R. Goldsmith, R. Ouyang, C. B. Musgrave, L. M. Ghiringhelli and M. Scheffler, *Sci. Adv.*, 2019, **5**, eaav0693.
20 G. Kieslich, S. Sun and A. K. Cheetham, *Chem. Sci.*, 2014, **5**, 4712.
21 Z. Li, M. Yang, J.-S. Park, S.-H. Wei, J. J. Berry and K. Zhu, *Chem. Mater.*, 2016, **28**, 284.
22 Q. Han, S.-H. Bae, P. Sun, Y.-T. Hsieh, Y. Yang, Y. S. Rim, H. Zhao, Q. Chen, W. Shi, G. Li and Y. Yang, *Adv. Mater.*, 2016, **28**, 2253.
23 T. Niu, J. Lu, M.-C. Tang, D. Barrit, D.-M. Smilgies, Z. Yang, J. Li, Y. Fan, T. Luo, I. McCulloch, A. Amassian, S. Liu and K. Zhao, *Energy Environ. Sci.*, 2018, **11**, 3358.
24 E. R. Dohner, E. T. Hoke and H. I. Karunadasa, *J. Am. Chem. Soc.*, 2014, **136**, 1718.
25 D. S. Wiersma, *Nat. Phys.*, 2008, **4**, 359.
26 B. Redding, M. A. Choma and H. Cao, *Nat. Photonics*, 2012, **6**, 355.
27 Q. Zhang, R. Su, X. Liu, J. Xing, T. C. Sum and Q. Xiong, *Adv. Funct. Mater.*, 2016, **26**, 6238.
28 G. Xing, N. Mathews, S. S. Lim, N. Yantara, X. Liu, D. Sabba, M. Grätzel, S. Mhaisalkar and T. C. Sum, *Nat. Mater.*, 2014, **13**, 476.
29 Q. Liao, K. Hu, H. Zhang, X. Wang, J. Yao and H. Fu, *Adv. Mater.*, 2015, **27**, 3405.
30 P. K. Roy, G. Haider, H.-I. Lin, Y.-M. Liao, C.-H. Lu, K.-H. Chen, L.-C. Chen, W.-H. Shih, C.-T. Liang and Y.-F. Chen, *Adv. Opt. Mater.*, 2018, **6**, 1800382.

31 Y. Hu, L. M. Spies, D. Alonso-Álvarez, P. Mocherla, H. Jones, J. Hanisch, T. Bein, P. R. F. Barnes and P. Docampo, *J. Mater. Chem. A*, 2018, **6**, 22215.
32 M. Anni, D. Rhee and W.-K. Lee, *ACS Appl. Mater. Interfaces*, 2019, **11**, 9385.
33 J. Wang, J. Li, S. Lan, C. Fang, H. Shen, Q. Xiong and D. Li, *ACS Nano*, 2019, **13**, 5473.
34 M. L. De Giorgi and M. Anni, *Appl. Sci.*, 2019, **9**, 4591.
35 P. Stano and P. Jacquod, *Nat. Photonics*, 2013, **7**, 66.
36 B. Liu, C. M. M. Soe, C. C. Stoumpos, W. Nie, H. Tsai, K. Lim, A. D. Mohite, M. G. Kanatzidis, T. J. Marks and K. D. Singer, *Sol. RRL*, 2017, **1**, 1700062.
37 A. L. Schawlow and C. H. Townes, *Phys. Rev.*, 1958, **112**, 1940.
38 H. Zhu, Y. Fu, F. Meng, X. Wu, Z. Gong, Q. Ding, M. V. Gustafsson, M. T. Trinh, S. Jin and X. Y. Zhu, *Nat. Mater.*, 2015, **14**, 636.
39 S. A. Veldhuis, P. P. Boix, N. Yantara, M. Li, T. C. Sum, N. Mathews and S. G. Mhaisalkar, *Adv. Mater.*, 2016, **28**, 6804.
40 B. R. Sutherland and E. H. Sargent, *Nat. Photonics*, 2016, **10**, 295.
41 J. Liu, P. D. Garcia, S. Ek, N. Gregersen, T. Suhr, M. Schubert, J. Mørk, S. Stobbe and P. Lodahl, *Nat. Nanotechnol.*, 2014, **9**, 285.
42 Y. Ling, H. Cao, A. L. Burin, M. A. Ratner, X. Liu and R. P. H. Chang, *Phys. Rev. A*, 2001, **64**, 063808.
43 H. Cao, Y. G. Zhao, S. T. Ho, E. W. Seelig, Q. H. Wang and R. P. H. Chang, *Phys. Rev. Lett.*, 1999, **82**, 2278.
44 H.-W. Hu, G. Haider, Y.-M. Liao, P. K. Roy, R. Ravindranath, H.-T. Chang, C.-H. Lu, C.-Y. Tseng, T.-Y. Lin, W.-H. Shih and Y.-F. Chen, *Adv. Mater.*, 2017, **29**, 1703549.
45 G. Haider, R. Ravindranath, T.-P. Chen, P. Roy, P. K. Roy, S.-Y. Cai, H.-T. Chang and Y.-F. Chen, *Nat. Commun.*, 2017, **8**, 256.